Letter

Half-quantized Hall effect and power law decay of edge-current distribution

Jin-Yu Zou, Bo Fu, Huan-Wen Wang, Zi-Ang Hu, and Shun-Qing Shen[*]
Department of Physics, The University of Hong Kong, Pokfulam Road, Hong Kong, China

(Received 10 February 2022; revised 8 April 2022; accepted 26 April 2022; published 6 May 2022)

Half-quantized Hall conductance is characteristic of quantum systems with the parity anomaly. Here, we investigate topological and transport properties of a class of parity anomalous semimetals, in which massive Dirac fermions coexist with massless Dirac fermions in momentum space or real space, and uncover a distinct bulk-edge correspondence in which the half-quantized Hall effect is realized via the bulk massless Dirac fermions while the nontrivial Berry curvature is provided by the massive Dirac fermions. The spatial distribution of the edge current decays away from the boundary according to a power law instead of an exponential law in the integer quantum Hall effect. We further address the physical relevance of parity anomalous semimetals to three-dimensional semimagnetic topological insulators and two-dimensional photonic crystals.

DOI: 10.1103/PhysRevB.105.L201106

Introduction. The two-component massless Dirac fermion in 2+1 dimensions coupled with an electromagnetic field A_μ is invariant under time-reversal and spatial reflection symmetry at the classical level but loses the symmetries when the theory is quantized in a gauge-invariant fashion. This phenomenon is known as the "parity anomaly" [1–5]. Upon integrating out the fermion field in the action by means of the Pauli-Villars regularization [3], a Chern-Simons term which is odd under reflection and time reversal arises in the effective Lagrangian for the gauge field: $\mathcal{L}_{\rm CS}[A_\mu] = \frac{\sigma_H}{2}\epsilon^{\mu\nu\rho}A_\mu\partial_\nu A_\rho$, with $\epsilon^{\mu\nu\rho}$ being the Levi-Civita symbol and $\sigma_H = \frac{1}{2}\frac{e^2}{h}\frac{M}{|M|}$ only depending on the sign of the mass M for the regulator. The Chern-Simons term predicts a half-quantized Hall conductance [6]. Several condensed matter systems were proposed to realize the parity anomaly in early pioneering works, such as the single-layer graphite system [7], the PbTe-type narrow gap semiconductor with a domain wall [8], and, recently, the HgTe heterostructure [9]. Haldane proposed that the half-quantized Hall conductance could be obtained if one of the two gapped valleys on a honeycomb lattice can be fine-tuned to be closed [10]. Recently, Haldane's idea has been constructed in photonic [11] and phononic [12,13] crystals, as well as Floquet systems [14,15]. Another attempt to realize the parity anomaly is based on the surface states of three-dimensional (3D) Z_2 topological insulators [6,16–20]. If the surface states are gapped by magnetic doping or the proximity effect at one surface of the system while the surface states at the opposite surface remain gapless, an unpaired gapless Dirac cone can be realized in the quasi-2D system with a lattice-regularized description [21–30]. Recently, this "semimagnetic" heterostructure was reported experimentally in Refs. [31,32]. As illustrated in Figs. 1(a) and 1(b), the massive and massless Dirac cones are separated in momentum space in the Haldane model and in position space in a semimagnetic topological insulator, which plays the role of the Pauli-Villars regulator, making them an ideal platform for the condensed matter realization of the "parity anomaly." Topological semimetals in which massive and massless Dirac fermions coexist are named "parity anomalous semimetals" [33,34], to emphasize the role of the massless Dirac fermions in the parity anomaly.

Opposite to the integer quantum Hall effect and quantum anomalous Hall effect [35,36], the half-quantized Hall effect does not indicate the existence of well-defined chiral edge states as the number of chiral edge states cannot be half of an integer and also the carrier charge is not a fraction of the elementary charge e in these noninteracting systems. In this Research Letter, we study electronic and transport properties of parity anomalous semimetals for the open boundary condition by means of a combination of analytical and numerical techniques. While no well-defined edge states are present, it is found that the accumulation of all extended bulk states exhibits chiral nature and an edge current circulates around the boundary as shown in Fig. 1(c). The edge current decays according to a power law of the distance x away from the boundary, $x^{-3/2}$, which is different from the exponential decay in the integer quantum Hall effect due to the presence of the localized edge states [19,37,38]. The circulating electric current generates a magnetization which leads to a half-quantized Hall conductance according to the Streda formula [39,40]. We also demonstrate the topological charge pumping from the collective contribution of the bulk extended states. Furthermore, we explore the Hall current distribution and charge pumping in a semimagnetic topological insulator slab, which provides a comprehensive and distinct physical picture of the half-quantized surface Hall effect.

Haldane model with parity anomaly. To demonstrate the distinct bulk-edge correspondence, we consider the Haldane model with armchair-type termination as illustrated in Fig. 2(a). To meet the boundary condition of the armchair termination, we must admix states of different valleys [41]. Effectively, the presence of the gapped valley behaves as a

[*]sshen@hku.hk

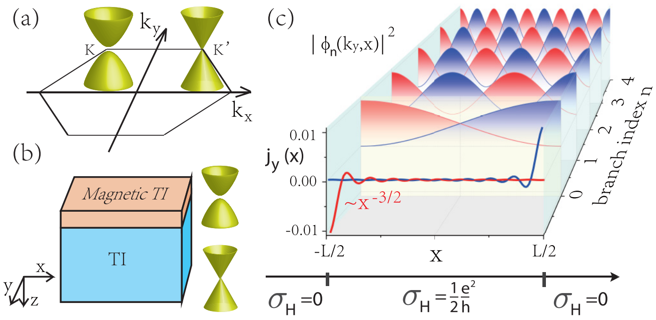

FIG. 1. Illustration of parity anomalous semimetals: (a) the Haldane model where massive and massless Dirac cones are separated in momentum space and (b) the semimagnetic 3D topological insulator (TI) in which massive and massless Dirac cones are separated in position space. (c) The distribution of a set of low-energy states and the power-law-decaying edge current in the parity anomalous semimetal with the half-quantized Hall conductance $\sigma_H = \frac{1}{2}\frac{e^2}{h}$ for the open boundary condition. The up- and down-propagating states are indicated by red and blue colors, respectively.

boundary condition for the envelope function of the gapless valley [42]. If we consider a low-energy scale which is much smaller than the gap of the massive valley, the confinement can be approximated as the hard-wall boundary condition, which was extensively discussed in previous studies [43–47]. In this approach, the energy eigenvalues are analytically solvable $\varepsilon_n(k_y) = \hbar v_F\sqrt{k_y^2 + [\frac{\pi}{L}(n+\frac{1}{2})]^2}$ ($n = 0, 1, 2, 3, \ldots$), with v_F being the Fermi velocity and L being the length of the ribbon. Due to the presence of factor $1/2$, there exists a finite energy gap inversely proportional to the ribbon width L, $\Delta = 2\hbar v_F\pi/L$. The numerical eigenvalues for the eigenenergy show good agreement with this analytic expression in the low-energy scale. The corresponding wave function with conserved momentum k_y can be written as $\Psi_n(x, y) = e^{ik_y y}|nk_y\rangle$, which are all extended states. However, we can calculate the average displacement relative to the center of the ribbon for each of the states $\langle nk_y|(\frac{x}{L} - \frac{1}{2})|nk_y\rangle = -\frac{\hbar v_F k_y}{\varepsilon_n(k_y)}\frac{2}{\pi^2(2n+1)^2}$, which is proportional to the propagation velocity. This result means that the down-propagating states located in the left half portion of the ribbon and the states located in the opposite portion flow in opposite directions [shown by the red and blue curves with filling color in Fig. 1(c), respectively]. To indicate this chiral nature, we calculate the local density of states at the boundary in Fig. 2(b). There is a remarkable asymmetry in the spectral weight between the left- and right-moving modes. As a consequence, there must be an equilibrium circulating current [48] in the sample for finite chemical potential. The transverse current density is given by $j_y(x) = e\sum_{k_y}^{\varepsilon_n(k_y)<\mu}\langle nk_y|\frac{1}{\hbar}\frac{\partial H}{\partial k_y}|nk_y\rangle$ for the occupied states [42]

$$j_y(x) = \frac{e}{h}\frac{\mu}{2}\sum_{s=\pm} s\frac{J_1(2k_F|x - R_s|)}{|x - R_s|}, \quad (1)$$

where μ is the chemical potential, $k_F = \mu/(\hbar v_F)$ is the Fermi wave vector, $J_n(x)$ is the first kind of Bessel function, and $R_{s=+} = 0$ or $R_{s=-} = L$ for the two edges $s = \pm$. By using the asymptotic form of $J_1(x)$ at a large argument x, we find that the edge current $j_y^s(x) \propto x^{-3/2}\cos(2k_F x - \frac{3\pi}{4})$ is maximized at the boundary and decays to zero according to a power law $\sim x^{-3/2}$ when moving away from the boundary with the oscillation length $1/(2k_F)$. This analytic result fits well with the numerical calculation as shown in Fig. 2(c). As μ increases, the oscillation length of $j_y^s(x)$ decreases. In a quantum anomalous Hall insulator or integer quantum Hall insulator, the localized edge states give an exponential decay behavior with the decaying length proportional to the inverse of the energy gap. This power law behavior of the equilibrium circulating current with the decay exponent $-3/2$ provides a fingerprint to identify the parity anomalous semimetal. The magnetization $\boldsymbol{M}$ induces a magnetization current density $\boldsymbol{j} = \nabla \times \boldsymbol{M}$. Inversely, the equilibrium current $j_y^s(x)$ corresponds to a spatially varied magnetization

$$M_z^s(x) = -\int_{R_+}^{x} dx'\, j_y^s(x') = -\frac{e}{h}\frac{\mu}{2}\mathcal{F}[2k_F(x - R_+)], \quad (2)$$

with $\mathcal{F}(x) = J_1'(x) + \frac{\pi x}{2}[J_1(x)H_0(x) - J_0(x)H_1(x)]$, where $H_n(x)$ are the Struve functions. $\mathcal{F}(x)$ has the asymptotic behaviors $\mathcal{F}(x) = x/2$ for a tiny $x \to 0$ and $\mathcal{F}(x) = 1$ for $x \to +\infty$. The magnetic field $B_z = \mu_0 M_z$ through the sample as a function of position should be measurable by magnetic flux detectors such as a superconducting quantum interference device (SQUID) [49]. After scanning the magnetic field with a SQUID, the position-dependent current is visualized. Our main result that parity anomalous

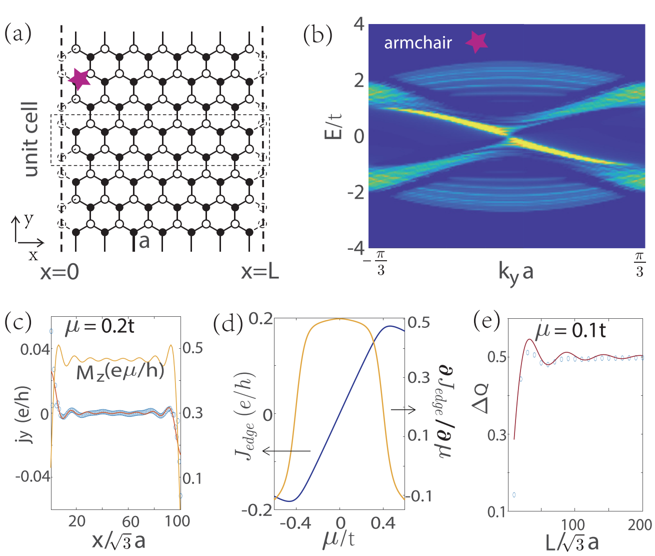

FIG. 2. (a) Structure of honeycomb lattice nanoribbons with armchair edges. a is the lattice distance. (b) The local density of states at the left edge (labeled by the star). Yellow color indicates higher values, and blue indicates lower values. (c) The distribution of current j_z and magnetization M_z with the Fermi level $\mu = 0.2t$. The circles and curves represent numerical and analytical results, respectively. (d) The edge current (blue curve) $J_{\rm edge} = \int_0^{L/2} dx\, j_y(x)$ and its derivative with respect to μ (yellow curve) as a function of μ. (e) The charge pumping ΔQ as a function of ribbon width L for a fixed μ. The circles and curve represent numerical and analytical [Eq. (3)] results, respectively.

semimetals host a power-law-decaying edge current thus can be experimentally measured by a SQUID. We plot the magnetization field $M_z = \sum_{s=\pm} M_z^s$ versus position x in an armchair ribbon by setting the origin at one edge shown as the yellow curve in Fig. 2(c). As we move from the edge, the magnetization M_z increases from 0 and then saturates to the bulk value with oscillation. Due to finite-size confinement along the x direction, the magnetization is not half quantized (in units of $e\mu/h$) when the ribbon is narrow. However, the bulk value of M_z converges quickly into the half-quantized value as $k_F L$ increases owing to the asymptotic behavior of $\mathcal{F}(x)$. The total equilibrium out-of-plane magnetization can be calculated thermodynamically, $M_z = -\partial_B \Omega(\mu, B)$, where B is the magnetic field and Ω is the grand-canonical thermodynamic potential of electrons at chemical potential μ. From the Maxwell relation, we have $\partial_\mu M_z = -\partial_\mu(\partial_B \Omega) = \partial_B(-\partial_\mu \Omega) = \partial_B \rho$, with ρ being the carrier density. In the thermodynamic limit $k_F L \to \infty$, the Hall response $\sigma_H = e\partial_\mu M_z = \frac{e^2}{2h}$ is half quantized according the Streda formula [39] $\sigma_H = e\partial_B \rho|_\mu$. The bulk magnetization can be obtained from the edge current $M_z^{\text{bulk}} = J_{\text{edge}} = \int_0^{L/2} dx\, j_y(x)$. As shown in Fig. 2(d), we plot the edge current J_{edge} as a function of the chemical potential in the armchair ribbon (blue curve). When the chemical potential is around the band-crossing point, the edge current displays a linear dependence of μ with a slope of $\sim e/2h$.

Charge pumping. We consider a cylinder with a circumference W along the y direction and with length L along the x direction, which is pierced by magnetic flux Φ. With changing magnetic field, an electric field along the circumferential direction can be induced according to Faraday's law, $E(t) = \frac{1}{W}\partial_t \Phi$. Due to the boundary confinement effect along the x direction, the energy spectrum for such a geometry becomes a series of discrete one-dimensional subbands ε_n. In the presence of the electric field, the acceleration of the electron is given by $\hbar\dot{k} = eE$. The magnetic flux is switched on adiabatically, which means that the rate of change of the flux is much smaller than the energy spacing between two bands $\hbar v_F \pi/L$, such that no particles are excited into the next subbands. Then the number of electrons with positive velocity increases, the number of electrons with negative velocity decreases, and the total number of electrons for each branch n is conserved. Over the interval time Δt, the change in the wave vector is $\frac{e}{\hbar}E\Delta t$. If the flux changes by one quantum flux $\Phi_0 = h/e$ over time Δt, we have $EW\Delta t = \Phi_0$. The spatial imbalance for each state is $\Delta\rho_n(k_x) = \langle nk_y|[\Theta(x) - \frac{1}{2}]|nk_y\rangle = \frac{\hbar v_F k_y}{\varepsilon_n(k_y)} \frac{\sin[\pi(n+1/2)]}{2\pi(n+1/2)}$, where $\Theta(x)$ is the step function. Thus the charge transfer from one side to the other can be expressed as the spatial imbalance difference between the two states with opposite velocity at the Fermi level $\Delta Q = \frac{e}{2}\sum_n[\Delta\rho_n(k_n^{f+}) - \Delta\rho_n(k_n^{f-})]$ [42], where we have assumed that the chemical potential μ lies in the gap of the gapped valley and intersects only with the gapless one and $k_n^{f\pm}$ are the two Fermi wave vectors for branch n. The summation over n is performed over all the branches intersecting the Fermi level and can be done analytically,

$$\Delta Q = -\frac{e}{2}\mathcal{F}(k_F L). \tag{3}$$

$\mathcal{F}(x) = 1$ for $x \to +\infty$. In Fig. 2(e), we plot the analytical expression [Eq. (3)] and the numerical results for the cylinder geometry as a comparison. Thus there is half charge pumping from the one edge to the other in the thermodynamic limit. The final expression for charge transfer (3) is a collective consequence of all the bands intersecting the Fermi level. It is in sharp contrast with a quantum anomalous Hall insulator, where the charge transfer is attributed from the two chiral edge states at the two sides [50–53]. Assuming that we have a system with the Hall conductance σ_H, we obtain the charge transferred as $\Delta Q = \sigma_H \Phi_0$. From Eq. (3), the Hall conductance is given by $\sigma_H = -\frac{e^2}{2h}\mathcal{F}(k_F L)$, which is identical to the expression derived from the magnetization (2) by setting x at the center of the ribbon. It indicates that the half charge pumping shares the same topological origin with the half-quantized quantum Hall effect.

For the zigzag boundary condition there exist localized states along the boundary, and this will slightly revise the picture [41]. For the extended states, the zigzag boundary condition will not admix two valleys. We can solve the enveloped functions for each valley separately and find that the spatial imbalance vanishes, $\Delta\rho_n(k_n^{f\pm}) = 0$, for all extended states. As for the localized edge states which connect two valleys, the boundary condition will strongly admix valley states. The localized states' solutions depend on the wave number and only exist in the lowest-energy branch $n = 0$. The positive Fermi vector corresponds to a localized state with $\Delta\rho_{n=0}(k_{n=0}^{f+}) = 1$, while the negative Fermi vector corresponds to an extended state with $\Delta\rho_{n=0}(k_{n=0}^{f-}) = 0$. Consequently, we have $\Delta Q = \frac{e}{2}\Delta\rho_{n=0}(k_{n=0}^{f+}) = \frac{e}{2}$ [42].

3D semimagnetic topological insulator. Another potential candidate for a parity anomalous semimetal is a 3D topological insulator coated on top by an insulating ferromagnetic material as shown in Fig. 3(a), now named a semimagnetic topological insulator [32]. The topological insulator hosts massless Dirac fermions around its surface. The states located at the interface between the topological insulator and the ferromagnet open an energy gap due to the proximity effect. Thus the massless Dirac fermions and massive Dirac fermions are separated in space but still have to coexist to form a semimetal as a whole because massive Dirac fermions alone are prohibited to exist independently. To illustrate the topological properties of the system, we can imagine unfolding the surfaces states into a flat 2D plane [54]: The gapless central region $|x| < L/2$ is sandwiched between the two gapped outer regions $|x| > L/2$. We plot the numerical results of the energy spectrum for the 3D semimagnetic topological insulator (colored dots) as a comparison with the analytical expression (black curves) in Fig. 3(b). We denote the bulk band gap by m and the surface band gap induced by the Zeeman field by B with $|B| < |m|$. Here, we only consider the physics in the energy window in which the chemical potential is located within the surface band gap $|B|$. The numerical and analytical results are in good agreement with each other in this low-energy region. Since the top and bottom surface Dirac cones are located at the same point in momentum space, their spectra and physical properties are an analog to the critical Haldane model with the armchair termination.

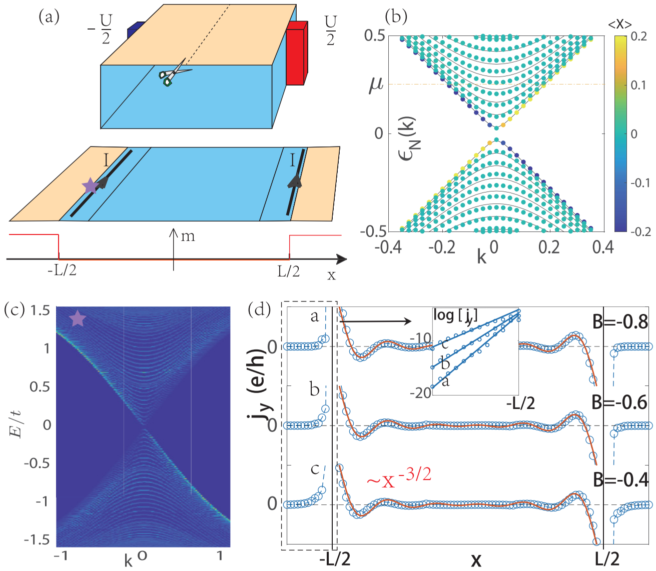

FIG. 3. (a) A slab of a three-dimensional topological insulator coated by an insulating ferromagnetic material (yellow region) on the top. When the voltage bias U is applied by the leads attached on the x terminals, net current I presents on the hinge. (b) Comparison of the numerical results of the spectrum of a 3D semimagnetic topological insulator for quasi-1D geometry (dots) and the analytic expression $\varepsilon_n(k) = \hbar v_F\sqrt{k^2 + [\frac{\pi}{L}(n+\frac{1}{2})]^2}$ (curves). The color represents the center of mass $\langle x/L\rangle$ for each state. (c) The local density of states at the top hinge at the position labeled with a star in (a). (d) The surface current distribution on the perimeter of the semimagnetic topological insulator bar for a fixed chemical potential $\mu = 0.15m$ and several different Zeeman fields $B = -0.2m$, $-0.3m$, and $-0.4m$ induced by the coated ferromagnetic material. The inset shows the $\log(j_y)$-x plot in the gapped region. The red curves are the analytic current distributions according to Eq. (1). We have chosen the bulk band gap m as the energy unit and $\hbar v_F = 0.7am$, with a being the lattice constant.

Due to the quasi-2D feature of the semimagnetic topological insulator, it will display some unique features distinct from the 2D system. One can also calculate the Hall conductance explicitly as a sum of the real-space-projected layer-resolved Hall conductance $C_z(l)$, $\sigma_{\rm H} = \sum_l C_z(l)e^2/h$ [42,55–59]. It is found that that nonzero $C_z(l)$ is mainly distributed near the interface and the integrated Hall conductance $\sigma_{\rm H} = e^2/2h$ [31,60]. To facilitate the numerical calculation, the chemical potential μ is set to deviate slightly from zero to avoid the degeneracy at zero energy due to the gapless bottom surface. Then we consider how the surface Hall conductance can be related to measurable physical quantities. The Hall conductance is evaluated with the periodic boundary condition in the xy plane. When we further impose the open boundary condition in the x direction, the quantum confinement effect forces the surface states into a series of subbands. We plot the local density of states of the top left hinge [labeled by the star in Fig. 3(a)] as shown in Fig. 3(c). The up-moving states show heavier spectral weight than the down-moving modes. Although all these modes are extended in the gapless region, they exhibit a chiral nature and carry a circulating hinge current from Eq. (1). As shown in Fig. 3(d), we plot the surface current distribution on the perimeter of the semimagnetic topological insulator bar for several Zeeman fields with fixed chemical potential. In the gapless region, both the current oscillation and asymptotic behavior $\sim|x+L/2|^{-3/2}$ of the envelope function can be well fitted by Eq. (1) (indicated by the red curves). In the gapped region, the current decays exponentially $\propto \exp(-\frac{2B}{\hbar v_F}|x+L/2|)$ from the interface. Thus the half-quantized Hall conductance can be associated with the appearance of circulating currents (no hinge modes) around the hinges. In the equilibrium case with a constant chemical potential, the total current integrated over the width of the sample is zero since the counterpropagating currents localized on the opposite edge cancel each other. The description of an equilibrium circulating current that changes its magnitude as a function of the chemical potential provides a useful framework for exploring the nonequilibrium phenomena. As shown in Fig. 3(a), in the presence of the external voltage bias U between two side surfaces [61], each branch of the confinement states generally has a different position-dependent chemical potential and nonequilibrium carrier distribution. There is a net drop eU in the chemical potential between two side surface states. From Eq. (1), the edge current is proportional to the chemical potential, the counterpropagating edge currents cannot compensate, and the total current becomes finite due to the voltage bias. The spatial distribution of the edge current on the side surface is consistent with the layer-resolved Hall conductance and thus can be viewed as its measurable physical quantity.

Discussion. At last, we give a brief discussion of the quantum anomalous Hall state and the "axion" state, which are realized in a topological insulator thin-film slab with a magnetic layer that is parallel and antiparallel, respectively, to both the top and bottom surfaces [62–66]. The former understanding is based on the Chern number calculation with periodic boundary condition and the total Hall conductance counts the the top and bottom surface together, yielding a $(1/2+1/2)$ or $(1/2-1/2)$ quantized value, respectively. However, this picture completely ignores the crucial effect from the lateral surface states when open boundary conditions are imposed. The proposed surface-state-unfolding analysis can also be applied to these two cases with both gapped top and bottom surfaces. In this situation, the gapless side surface is sandwiched between the two gapped regions with the same or opposite mass depending on the relative magnetic orientation of the two surfaces. Therefore the side surface states for an axion insulator share the same solutions as for a parity anomalous semimetal. For the quantum anomalous Hall state, the eigenvalues for side surface states are found to be $\varepsilon_n^{\rm QAH}(k_y) = \hbar v_F\sqrt{k_y^2 + [\frac{\pi}{L}n]^2}$ for $n \geqslant 1$ and $\varepsilon_n^{\rm QAH}(k_y) = \hbar v_F k_y$ for $n = 0$ [42]. The chiral state $n = 0$ is distributed uniformly in the gapless side surface and thus can be viewed as the generalized Jackiw-Rebbi solution for a mass domain wall [67]. Since the chiral modes always coexist with unchiral modes for finite chemical potential, it is found that the edge current shares the same expression as for a parity anomalous semimetal [Eq. (1)] except for the reverse of the current at one interface. This result implies that the power-law-decaying edge current is a local property at the interface between gapped and gapless regions in which the Hall conductances differ by one-half quantum. As seen from analytic exact solutions, the integer quantization for the quantum anomalous Hall state and the zero Hall plateau for the axion state can be understood in a unified and comprehensive way from the aspect of the parity anomalous semimetal.

Acknowledgments. This work was supported by the National Key R&D Program of China under Grant No. 2019YFA0308603 and the Research Grants Council, University Grants Committee, Hong Kong, under Grants No. C7012-21G and No. 17301220.

J.-Y.Z. and B.F. contributed equally to this work.

[1] A. J. Niemi and G. W. Semenoff, Axial-Anomaly-Induced Fermion Fractionization and Effective Gauge-Theory Actions in Odd-Dimensional Space-Times, Phys. Rev. Lett. **51**, 2077 (1983).

[2] R. Jackiw, Fractional charge and zero modes for planar systems in a magnetic field, Phys. Rev. D **29**, 2375 (1984).

[3] A. N. Redlich, Gauge Noninvariance and Parity Nonconservation of Three-Dimensional Fermions, Phys. Rev. Lett. **52**, 18 (1984).

[4] D. Boyanovsky, R. Blankenbecler, and R. Yahalom, Physical origin of topological mass in 2 + 1 dimensions, Nucl. Phys. B **270**, 483 (1986).

[5] A. M. J. Schakel, Relativistic quantum Hall effect, Phys. Rev. D **43**, 1428 (1991).

[6] X.-L. Qi, T. L. Hughes, and S.-C. Zhang, Topological field theory of time-reversal invariant insulators, Phys. Rev. B **78**, 195424 (2008).

[7] G. W. Semenoff, Condensed-Matter Simulation of a Three-Dimensional Anomaly, Phys. Rev. Lett. **53**, 2449 (1984).

[8] E. Fradkin, E. Dagotto, and D. Boyanovsky, Physical Realization of the Parity Anomaly in Condensed Matter Physics, Phys. Rev. Lett. **57**, 2967 (1986).

[9] J. Böttcher, C. Tutschku, L. W. Molenkamp, and E. M. Hankiewicz, Survival of the Quantum Anomalous Hall Effect in Orbital Magnetic Fields as a Consequence of the Parity Anomaly, Phys. Rev. Lett. **123**, 226602 (2019).

[10] F. D. M. Haldane, Model for a Quantum Hall Effect without Landau Levels: Condensed-Matter Realization of the Parity Anomaly, Phys. Rev. Lett. **61**, 2015 (1988).

[11] G.-G. Liu, P. Zhou, Y. Yang, H. Xue, X. Ren, X. Lin, H.-x. Sun, L. Bi, Y. Chong, and B. Zhang, Observation of an unpaired photonic Dirac point, Nat. Commun. **11**, 1873 (2020).

[12] J. Lu, C. Qiu, L. Ye, X. Fan, M. Ke, F. Zhang, and Z. Liu, Observation of topological valley transport of sound in sonic crystals, Nat. Phys **13**, 369 (2017).

[13] Y. Ding, Y. Peng, Y. Zhu, X. Fan, J. Yang, B. Liang, X. Zhu, X. Wan, and J. Cheng, Experimental Demonstration of Acoustic Chern Insulators, Phys. Rev. Lett. **122**, 014302 (2019).

[14] H. Hu, W.-Y. Tong, Y.-H. Shen, X. Wan, and C.-G. Duan, Concepts of the half-valley-metal and quantum anomalous valley Hall effect, npj Comput. Mater. **6**, 129 (2020).

[15] D. Leykam, M. C. Rechtsman, and Y. D. Chong, Anomalous Topological Phases and Unpaired Dirac Cones in Photonic Floquet Topological Insulators, Phys. Rev. Lett. **117**, 013902 (2016).

[16] L. Fu, C. L. Kane, and E. J. Mele, Topological Insulators in Three Dimensions, Phys. Rev. Lett. **98**, 106803 (2007).

[17] M. Z. Hasan and C. L. Kane, Colloquium: Topological insulators, Rev. Mod. Phys. **82**, 3045 (2010).

[18] X.-L. Qi and S.-C. Zhang, Topological insulators and superconductors, Rev. Mod. Phys. **83**, 1057 (2011).

[19] S. Q. Shen, *Topological Insulators*, Springer Series of Solid State Science, Vol. 174 (Springer, Heidelberg, 2012).

[20] C. X. Liu, X. L. Qi, H. J. Zhang, X. Dai, Z. Fang, and S. C. Zhang, Model Hamiltonian for topological insulators, Phys. Rev. B **82**, 045122 (2010).

[21] D.-H. Lee, Surface States of Topological Insulators: The Dirac Fermion in Curved Two-Dimensional Spaces, Phys. Rev. Lett. **103**, 196804 (2009).

[22] R. L. Chu, J. R. Shi, and S. Q. Shen, Surface edge state and half-quantized Hall conductance in topological insulators, Phys. Rev. B **84**, 085312 (2011).

[23] G. Rosenberg, H.-M. Guo, and M. Franz, Wormhole effect in a strong topological insulator, Phys. Rev. B **82**, 041104(R) (2010).

[24] K. Nomura and N. Nagaosa, Surface-Quantized Anomalous Hall Current and the Magnetoelectric Effect in Magnetically Disordered Topological Insulators, Phys. Rev. Lett. **106**, 166802 (2011).

[25] C. Brüne, C. X. Liu, E. G. Novik, E. M. Hankiewicz, H. Buhmann, Y. L. Chen, X. L. Qi, Z. X. Shen, S. C. Zhang, and L. W. Molenkamp, Quantum Hall Effect from the Topological Surface States of Strained Bulk HgTe, Phys. Rev. Lett. **106**, 126803 (2011).

[26] M. Mulligan and F. J. Burnell, Topological insulators avoid the parity anomaly, Phys. Rev. B **88**, 085104 (2013).

[27] E. J. König, P. M. Ostrovsky, I. V. Protopopov, I. V. Gornyi, I. S. Burmistrov, and A. D. Mirlin, Half-integer quantum Hall effect of disordered Dirac fermions at a topological insulator surface, Phys. Rev. B **90**, 165435 (2014).

[28] S. Zhang, L. Pi, R. Wang, G. Yu, X.-C. Pan, Z. Wei, J. Zhang, C. Xi, Z. Bai, F. Fei, M. Wang, J. Liao, Y. Li, X. Wang, F. Song, Y. Zhang, B. Wang, D. Xing, and G. Wang, Anomalous quantization trajectory and parity anomaly in Co cluster decorated $BiSbTeSe_2$ nanodevices, Nat. Commun. **8**, 977 (2017).

[29] M. F. Lapa, Parity anomaly from the Hamiltonian point of view, Phys. Rev. B **99**, 235144 (2019).

[30] A. A. Burkov, Dirac fermion duality and the parity anomaly, Phys. Rev. B **99**, 035124 (2019).

[31] R. Lu, H. Sun, S. Kumar, Y. Wang, M. Gu, M. Zeng, Y.-J. Hao, J. Li, J. Shao, X.-M. Ma, Z. Hao, K. Zhang, W. Mansuer, J. Mei, Y. Zhao, C. Liu, K. Deng, W. Huang, B. Shen, K. Shimada *et al.*, Half-Magnetic Topological Insulator with Magnetization-Induced Dirac Gap at a Selected Surface, Phys. Rev. X **11**, 011039 (2021); **11**, 029902(E) (2021).

[32] M. Mogi, Y. Okamura, M. Kawamura, R. Yoshimi, K. Yasuda, A. Tsukazaki, K. S. Takahashi, T. Morimoto, N. Nagaosa, M. Kawasaki, Y. Takahashi, and Y. Tokura, Experimental signature of the parity anomaly in a semi-magnetic topological insulator, Nat. Phys. **18**, 390 (2022).

[33] B. Fu, J.-Y. Zou, Z.-A. Hu, H.-W. Wang, and S.-Q. Shen, Quantum anomalous semimetals, arXiv:2203.00933 [cond-mat.mes-hall].

[34] H.-W. Wang, Bo Fu, J.-Y. Zou, Z.-A. Hu, and S.-Q. Shen, Fractional electromagnetic response in three-dimensional chiral anomalous semimetal, arXiv:2202.01957 [cond-mat.mes-hall].

[35] D. J. Thouless, M. Kohmoto, M. P. Nightingale, and M. den Nijs, Quantized Hall Conductance in a Two-Dimensional Periodic Potential, Phys. Rev. Lett. **49**, 405 (1982).

[36] Y. Hatsugai, Chern Number and Edge States in the Integer Quantum Hall Effect, Phys. Rev. Lett. **71**, 3697 (1993).

[37] R. S. K. Mong and V. Shivamoggi, Edge states and the bulk-boundary correspondence in Dirac Hamiltonians, Phys. Rev. B **83**, 125109 (2011).

[38] W. Vandenberghe and M. Fischetti, Imperfect two-dimensional topological insulator field-effect transistors, Nat. Commun. **8**, 14184 (2017).

[39] P. Streda, Quantised Hall effect in a two-dimensional periodic potential, J. Phys. C: Solid State Phys. **15**, L1299 (1982).

[40] N. A. Sinitsyn, A. H. MacDonald, T. Jungwirth, V. K. Dugaev, and J. Sinova, Anomalous Hall effect in a two-dimensional Dirac band: The link between the Kubo-Streda formula and the semiclassical Boltzmann equation approach, Phys. Rev. B **75**, 045315 (2007).

[41] L. Brey and H. A. Fertig, Electronic states of graphene nanoribbons studied with the Dirac equation, Phys. Rev. B **73**, 235411 (2006).

[42] See Supplemental Material at http://link.aps.org/supplemental/10.1103/PhysRevB.105.L201106 for details of the layer-resolved Hall conductance for a semimagnetic topological insulator (Sec. S1), analytical results for the surface states of a three-dimensional topological insulator (Sec. S2), and analytical results for the Haldane model (Sec. S3), which includes Refs. [10,19,20,41,43,44,55–57,59,61,68].

[43] M. V. Berry and R. J. Mondragon, Neutrino billiards: time-reversal symmetry-breaking without magnetic fields, Proc. R. Soc. Lond. A **412**, 53 (1987).

[44] E. McCann and V. I. Fal'ko, Symmetry of boundary conditions of the Dirac equation for electrons in carbon nanotubes, J. Phys.: Condens. Matter **16**, 2371 (2004).

[45] J. Tworzydł o, B. Trauzettel, M. Titov, A. Rycerz, and C. W. J. Beenakker, Sub-Poissonian Shot Noise in Graphene, Phys. Rev. Lett. **96**, 246802 (2006)

[46] G. J. Ferreira and D. Loss, Magnetically Defined Qubits on 3D Topological Insulators, Phys. Rev. Lett. **111**, 106802 (2013).

[47] B. M. Resende, F. C. Lima, R. H. Miwa, E. Vernek, and G. J. Ferreira, Confinement and fermion doubling problem in Dirac-like Hamiltonians, Phys. Rev. B **96**, 161113(R) (2017).

[48] M. Büttiker, Edge-State Physics Without Magnetic Fields, Science **325**, 278 (2009).

[49] A. Uri, Y. Kim, K. Bagani, C. K. Lewandowski, S. Grover, N. Auerbach, E. O. Lachman, Y. Myasoedov, T. Taniguchi, K. Watanabe, J. Smet, and E. Zeldov, Nanoscale imaging of equilibrium quantum Hall edge currents and of the magnetic monopole response in graphene, Nat. Phys. **16**, 164 (2020).

[50] R. B. Laughlin, Quantized Hall conductivity in two dimensions, Phys. Rev. B **23**, 5632 (1981).

[51] B. I. Halperin, Quantized Hall conductance, current-carrying edge states, and the existence of extended states in a two-dimensional disordered potential, Phys. Rev. B **25**, 2185 (1982).

[52] D. J. Thouless, Quantization of particle transport, Phys. Rev. B **27**, 6083 (1983).

[53] Q. Niu and D. J. Thouless, Quantised adiabatic charge transport in the presence of substrate disorder and many-body interaction, J. Phys. A: Math. Gen. **17**, 2453 (1984).

[54] K. Hattori and H. Okamoto, Chiral Surface Modes in Three-Dimensional Topological Insulators, J. Phys. Soc. Jpn. **85**, 053707 (2016).

[55] A. M. Essin, J. E. Moore, and D. Vanderbilt, Magnetoelectric Polarizability and Axion Electrodynamics in Crystalline Insulators, Phys. Rev. Lett. **102**, 146805 (2009).

[56] S. K. M. Roger, M. E. Andrew, and E. M. Joel, Antiferromagnetic topological insulators, Phys. Rev. B **81**, 245209 (2010).

[57] M. Sitte, A. Rosch, E. Altman, and L. Fritz, Topological Insulators in Magnetic Fields: Quantum Hall Effect and Edge Channels with a Nonquantized θ Term, Phys. Rev. Lett. **108**, 126807 (2012).

[58] J. Wang, B. Lian, X.-L. Qi, and S.-C. Zhang, Quantized topological magnetoelectric effect of the zero-plateau quantum anomalous Hall state, Phys. Rev. B **92**, 081107(R) (2015).

[59] A. Y. Gao, Y. F. Liu, C. W. Hu, J. X. Qiu *et al.*, Layer Hall effect in a 2D topological axion antiferromagnet, Nature (London) **595**, 521 (2021).

[60] M. Gu, J. Li, H. Sun, Y. Zhao, C. Liu, J. Liu, H. Lu, and Q. Liu, Spectral signatures of the surface anomalous Hall effect in magnetic axion insulators, Nat. Commu. **12**, 3524 (2021).

[61] D. Tong, The Quantum Hall Effect, arXiv:1606.06687.

[62] M. Mogi, M. Kawamura, R. Yoshimi, A. Tsukazaki, Y. Kozuka, N. Shirakawa, K. S. Takahashi, M. Kawasaki, and Y. Tokura, A magnetic heterostructure of topological insulators as a candidate for an axion insulator, Nat. Mater. **16**, 516 (2017).

[63] M. Mogi, M. Kawamura, A. Tsukazaki, R. Yoshimi, K. S. Takahashi, M. Kawasaki, and Y. Tokura, Tailoring tricolor structure of magnetic topological insulator for robust axion insulator, Sci. Adv. **3**, eaao1669 (2017).

[64] D. Xiao, J. Jiang, J.-H. O. Shin, W. Wang, F. Wang, Y.-F. Zhao, C. Liu, W. Wu, M. H. W. Chan, and N. Samarth, and C.-Z. Chang, Realization of the Axion Insulator State in Quantum Anomalous Hall Sandwich Heterostructures, Phys. Rev. Lett. **120**, 056801 (2018).

[65] D. Zhang, M. Shi, T. Zhu, D. Xing, and H. Zhang, and J. Wang, Topological Axion States in the Magnetic Insulator $MnBi_2Te_4$ with the Quantized Magnetoelectric Effect, Phys. Rev. Lett. **122**, 206401 (2019).

[66] C. Liu, Y. Wang, H. Li, Y. Wu, Y. Li, J. Li, K. He, Y. Xu, J. Zhang, and Y. Wang, Robust axion insulator and Chern insulator phases in a two-dimensional antiferromagnetic topological insulator, Nat. Mat. **19**, 522 (2020).

[67] R. Jackiw and C. Rebbi, Solitons with fermion number 1/2, Phys. Rev. D **13**, 3398 (1976).

[68] M. Ezawa, Valley-Polarized Metals and Quantum Anomalous Hall Effect in Silicene, Phys. Rev. Lett. **109**, 055502 (2012).